Chemical Science

ROYAL SOCIETY OF CHEMISTRY

EDGE ARTICLE

View Article Online
View Journal | View Issue

Cite this: *Chem. Sci.*, 2023, **14**, 13825

All publication charges for this article have been paid for by the Royal Society of Chemistry

Received 22nd August 2023
Accepted 9th November 2023

DOI: 10.1039/d3sc04424f

rsc.li/chemical-science

^{18}F-Labeled brain-penetrant EGFR tyrosine kinase inhibitors for PET imaging of glioblastoma†

Maruthi Kumar Narayanam,[ab] Jonathan E. Tsang,[a] Shili Xu,[ab] David A. Nathanson[a] and Jennifer M. Murphy *[ab]

Significant evidence suggests that the failure of clinically tested epidermal growth factor receptor (EGFR) tyrosine kinase inhibitors (*e.g.* erlotinib, lapatinib, gefitinib) in glioblastoma (GBM) patients is primarily attributed to insufficient brain penetration, resulting in inadequate exposure to the targeted cells. Molecular imaging tools can facilitate GBM drug development by visualizing drug biodistribution and confirming target expression and localization. To assess brain exposure *via* PET molecular imaging, we synthesized fluorine-18 isotopologues of two brain-penetrant EGFR tyrosine kinase inhibitors developed specifically for GBM. Adapting our recently reported radiofluorination of *N*-arylsydnones, we constructed an *ortho*-disubstituted [^{18}F]fluoroarene as the key intermediate. The radiotracers were produced on an automated synthesis module in 7–8% activity yield with high molar activity. *In vivo* PET imaging revealed rapid brain uptake in rodents and tumor accumulation in an EGFR-driven orthotopic GBM xenograft model.

Introduction

The epidermal growth factor receptor (EGFR) plays an important role in the development and progression of a variety of malignant tumors including glioblastoma (GBM), one of the most lethal malignancies with a median survival of approximately 16 months.[1] Novel anti-tumor therapies that target the ATP-binding site of the tyrosine kinase domain of EGFR have become popular and have resulted in the development of several tyrosine kinase inhibitors (TKIs), with some demonstrating significant clinical efficacy in EGFR mutant lung cancer.[2] By contrast, in GBM, first- and second-generation EGFR TKIs have failed to improve outcomes for these patients.[3] Their limited efficacy is largely attributed to the presence of a physical barrier – the blood–brain barrier (BBB) – which precludes the delivery of more than 98% of all therapeutics.[4] To achieve therapeutic efficacy in GBM, BBB permeability is considered an essential property to maximize patient benefit and clinical outcome.

Positron emission tomography (PET) molecular imaging provides a unique opportunity to non-invasively study disease and has contributed a key role in accelerating drug development, particularly in the fields of neurology and oncology.[5] The availability of a radiolabeled isotopologue of the small molecule drug candidate in the early stage of CNS drug development can provide information on whole body biodistribution, pharmacokinetics and target engagement.[5b,6] In the context of GBM, where brain penetration of drugs is critical, molecular imaging enables non-invasive measurements of differences between brain and plasma pharmacokinetics, indispensable data to establish the optimal therapeutic dose.[7] To date, several small molecule TKIs have been radiolabeled and evaluated as PET tracers in an effort to noninvasively assess the *in vivo* pharmacological properties of the drug.[8]

Radiotracers based on clinically approved TKIs have been described, two of which have been labeled with fluorine-18: ^{18}F-Gefitinib and ^{18}F-Afatinib (Fig. 1).[8e] Gefitinib, a first-generation

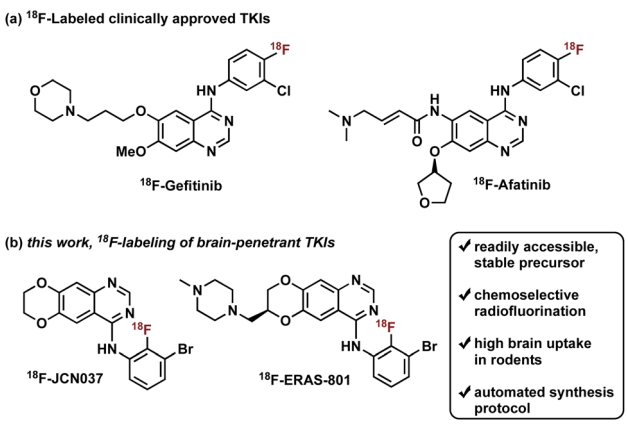

Fig. 1 (a) ^{18}F-Labeled tracers based on clinically approved tyrosine kinase inhibitors. (b) *This work*, synthesis and *in vivo* imaging of ^{18}F-JCN037 and ^{18}F-ERAS-801, potent brain-penetrant tyrosine kinase inhibitors.

[a]*Department of Molecular and Medical Pharmacology, David Geffen School of Medicine, University of California, Los Angeles, CA, 90095, USA*

[b]*Crump Institute for Molecular Imaging, David Geffen School of Medicine, University of California, Los Angeles, CA, 90095, USA. E-mail: jmmurphy@mednet.ucla.edu*

† Electronic supplementary information (ESI) available. See DOI: https://doi.org/10.1039/d3sc04424f

EGFR TKI approved for the treatment of advanced NSCLC, was radiolabeled with fluorine-18 in three steps, in a decay-corrected radiochemical yield (RCY) of 17%.[9] Preclinical *in vivo* studies with the radiotracer revealed limited brain penetration and a lack of uptake in EGFR-expressing tumor xenografts, which is consistent with human clinical experience with gefitinib treatment.[2b,8a,8b,10] Of note, a one-step synthesis of ^{18}F-Gefitinib was recently reported *via* Cu-mediated fluorination of the corresponding aryl pinacol borane with a 22% radiochemical conversion based on radio-TLC and radio-HPLC analysis of the crude material.[11] Afatinib, a second-generation EGFR TKI, is an irreversible inhibitor that contains a Michael acceptor for covalent conjugation to a cysteine residue in the ATP binding domain of EGFR (Fig. 1).[8e] Synthesis of ^{18}F-Afatinib utilizes a similar approach to that of ^{18}F-Gefitinib with a slight difference in the third step which employs a BOP-mediated condensation reaction with the 4-quinazolinone core.[12] Construction of ^{18}F-Afatinib was achieved in 17% RCY (decay-corrected) and *in vivo* evaluation in preclinical studies demonstrated similarly low brain uptake.[12,13] Of note, a feasibility study of ^{18}F-Afatinib in NSCLC patients was recently reported.[8d]

To address the pharmacological problem of current TKIs for the treatment of EGFR-driven GBMs, potent EGFR TKIs designed specifically to penetrate the BBB, JCN037 and its clinical derivative ERAS-801, have been developed that are both highly selective for extracellular domain mutant (*e.g.*, EGFRvIII) and amplified WT EGFR, alterations in EGFR that are specific to GBM.[14] These novel TKIs exhibit the 4-anilinoquinazoline core of clinically approved gefitinib and afatinib but incorporate a ring fusion of the 6,7-dialkoxy groups as well as a *meta*-bromine and *ortho*-fluorine on the aniline ring (Fig. 1). The structural modifications of JCN037 and ERAS-801, relative to TKIs erlotinib and lapatinb, resulted in considerably improved potency and BBB penetration. Superior efficacy was demonstrated in a GBM orthotopic patient-derived xenograft model (GliomaPDOX) where JCN037 was shown to significantly extend the survival of EGFR-altered, tumor-bearing mice.[14a] Notably, ERAS-801 which contains an *N*-methylpiperazine moiety is currently being investigated in phase I clinical trials for treatment of patients with GBM (NCT05222802).

We rationalized that a PET tracer for these TKIs could enable noninvasive measurements of drug biodistribution and accumulation and, importantly, inform on BBB penetration, providing key data largely responsible for the predictive measure of therapeutic efficacy and success. In this work, we report the synthesis and *in vivo* biodistribution of fluorine-18 isotopologues of JCN037 and ERAS-801, namely **^{18}F-JCN037** and **^{18}F-ERAS-801** (Fig. 1). To avoid differences in their *in vivo* behavior, the radiotracer and the parent compound have exactly the same chemical structure and, as a result, identical biodistribution, affinity, lipophilicity, polar surface area, *etc.* Additionally, *in vivo* imaging was conducted in EGFR-altered GliomaPDOX to evaluate target expression and accumulation of **^{18}F-ERAS-801** in EGFR-driven tumors. We anticipate this novel radiotracer could provide unique insights into the intratumoral drug distribution in the brain for EGFR-driven GBM tumors and facilitate clinical development.

Results and discussion

Radiosynthetic strategy

Construction of these radiotracers was envisioned to arise from the conventional S_NAr between aniline **^{18}F-2** and the 4-chloroquinazoline pharmacophore **3** to forge the key carbon–nitrogen bond (Scheme 1). The 4-chloroquinazoline core for **^{18}F-JCN037** and **^{18}F-ERAS-801** could be synthesized following literature protocol; thus, to achieve our goal, the critical synthetic step would be generation of radiolabeled aniline **^{18}F-2**.[14]

A particularly noteworthy characteristic of **^{18}F-2** is that it exhibits a sterically hindered *ortho*-disubstituted [^{18}F]fluoroaryl moiety which is a considerable synthetic challenge. Radiolabeling methodologies that tolerate bulky substituents *ortho* to the reactive site are limited with few examples of *ortho*-disubstituted [^{18}F]fluoroarenes in the literature.[15] We have previously reported the nucleophilic radiofluorination of *N*-arylsydnones which facilitates large *ortho*-substitution and readily affords [^{18}F]fluoroarenes in high yields.[16] Utilizing this methodology, we proposed to generate **^{18}F-2** *via* radiofluorination of the corresponding sydnone **1** followed by Pd-catalyzed reduction (Scheme 1).

First, we began our synthetic strategy with preparation of 2-bromo-6-nitrophenyl sydnone precursor **1** as shown in Scheme 2. Formation of the *N*-aryl glycine **5** was accomplished in 79% yield *via* S_NAr with bromo-2-fluoro-3-nitrobenzene **4**. The *N*-aryl glycine was converted to the corresponding nitrosamine with *t*butyl nitrate followed by cyclodehydration to form the sydnone **1** in 72% yield from **5**.

We initially evaluated various conditions for radiofluorination of precursor **1** directly on an automated radiosynthesis module (Table S1†). Given the strong activating nature of the *ortho*-nitro substituent towards S_NAr, conversion of precursor **1** to **^{18}F-4** was nearly quantitative after 10 min at 70 °C (Table 1). Investigation of lower temperatures revealed that the radiofluorination proceeded efficiently at 30 °C in 8 min to cleanly afford the desired nitrobenzene **^{18}F-4** in 97% RCY.

We next sought to prepare aniline **^{18}F-2**. Formation of **^{18}F-2** proceeded in 48% RCY upon the reduction of **^{18}F-4** in methanol with $NaBH_4$ in the presence of Pd/C at ambient temperature for 5 min (Table 2, entry 1). We first focused on the amounts of Pd/C and $NaBH_4$, keeping a consistent ratio of around 2- to 3-fold excess reducing agent over transition metal (Table 2, entries 1–4). Lowering the mass amount of $NaBH_4$ provided cleaner HPLC traces with less side product formation. Significantly lowering the mass of palladium was unproductive and completely suppressed the reduction (see Table 2, entry 4).

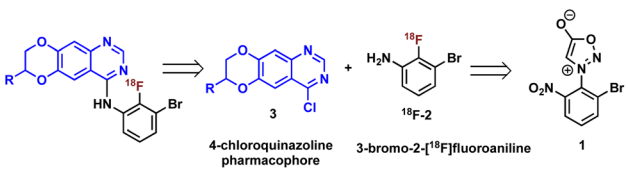

Scheme 1 Retrosynthetic analysis.

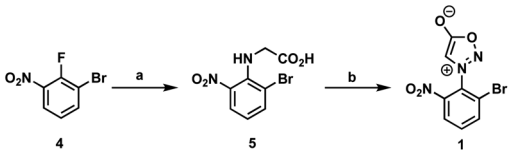

Scheme 2 Synthesis of 2-bromo-6-nitrophenyl sydnone **1**. Reagents and conditions: (a) glycine, K_2CO_3, 1,4-dioxane : water (1 : 3), 16 h, 50 °C, 79%; (b) *tert*-butyl nitrite, THF, 3 h, 23 °C; trifluoroacetic anhydride, 4 h, 23–40 °C, 72%.

Table 1 Optimization of radiofluorination to prepare 18F-4[a]

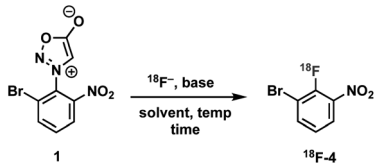

Entry[b]	Base	Solvent	Time (min)	Temp. (°C)	RCY[c] (%)
1	K_{222}/K_2CO_3	DMSO	10	70	96
2	Et_4NHCO_3	DMSO	10	70	96
3	**K_{222}/K_2CO_3**	**DMSO**	**8**	**30**	**97**
4	Et_4NHCO_3	DMSO	8	30	70
5	K_{222}/K_2CO_3	CH_3CN	8	30	65

[a] Conditions: sydnone precursor **1** (~1.5 mg), base (K_{222} (12 mg)/K_2CO_3 (2 mg) or Et_4NHCO_3 (4.2 mg)), [^{18}F]fluoride, solvent (400 μL). [b] Conducted on the ELIXYS automated radiosynthesis module. [c] RCY was determined by radio-TLC analysis of the crude product **^{18}F-4**.

Table 2 Optimization of reduction step to prepare ^{18}F-2[a]

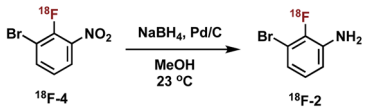

Entry	Pd/C (mg)	$NaBH_4$ (mg)	Time (s)	RCY[b] (%)
1	5.0	15.0	300	48
2	5.0	13.0	300	58
3	4.6	10.8	300	53
4	1.4	5.0	300	1
5	5.2	3.5	150	70
6	5.2	3.0	160	60
7	5.5	4.1	160	74
8	5.5	4.0	140	61
9	**5.2**	**4.6**	**150**	**85**
10	4.8	4.6	150	80

[a] Conditions: **^{18}F-4** (~185 MBq), methanol (1.2–1.5 mL), 23 °C. [b] RCY was determined by radio-HPLC analysis of the crude product **^{18}F-2**.

Altering the mass ratios between the reducing agent and transition metal to where the palladium was in slight excess proved to further minimize undesirable side product formation and provide cleaner product composition in half the reaction time (see Table S3†). In 2.5 min, conversion to **^{18}F-2** was achieved in 60–70% RCY with ~3 mg $NaBH_4$ and 5.2 mg Pd/C (Table 2, entries 5 and 6). Further refinement continued to improve the conversion and generate **^{18}F-2** in 85% RCY within 2.5 min (Table 2, entry 9).

With aniline **^{18}F-2** in hand, we focused on the substitution reaction with 4-chloroquinazoline **3a** to produce **^{18}F-JCN037** and rigorous screening was conducted. Initially, we used crude **^{18}F-2**, without further purification, and found that the addition of **3a** into the reaction vial in two equal portions, with the second portion being added after 15 min, revealed greater consumption of **^{18}F-2** and increased product formation (Table S6†). Therefore, a two-part addition of **3a** was continued throughout the optimization process. Product formation was observed in 41% RCY upon treatment of crude **^{18}F-2** with 1.3 mg of **3a** in IPA at 95 °C for 20 min (Table 3, entry 1). Screening solvents revealed IPA to be superior and increasing the mass amount of 4-chloroquinazoline **3a** yielded slightly higher RCYs (Table 3, entries 2–5).

Intermediate HPLC purification of **^{18}F-2** was briefly investigated, generating **^{18}F-JCN037** in 95% RCY albeit adding excessive time constraints to the overall process (Table S7†). Alternatively, to avoid the lengthy HPLC purification, C18 Sep-Pak cartridge purification of **^{18}F-2** was pursued. In IPA, **^{18}F-JCN037** was generated in 76% RCY upon treatment of cartridge-purified **^{18}F-2** with 5.0 mg of **3a** in IPA at 95 °C for 30 min (Table 3, entry 7). When this step was translated to an automated radiosynthesis module, the moderate solubility of 4-chloroquinazoline **3a** in IPA created an unsatisfactory heterogeneous reagent mixture. Alternatively, solubility of **3a** in acetonitrile enabled the consistent and complete addition of

Table 3 Optimization of S_NAr step to prepare ^{18}F-JCN037[a]

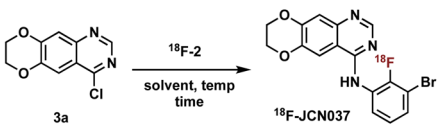

Entry	**3a** (mg)	Temp. (°C)	Solvent	Time (min)	RCY[b] (%)
1[c]	1.3	95	IPA	20	41
2[c]	1.3	95	DMF	25	30
3[c]	3.3	95	IPA	20	45
4[c]	3.6	95	MeOH	25	35
5[c]	5.5	95	IPA	25	49
6	3.5	95	IPA	30	58
7	5.0	95	IPA	30	76
8	4.5[d]	95	MeOH	30	65
9	5.5[d]	95	CH3CN	30	75
10	**5.0[d]**	**100**	**CH_3CN**	**30**	**78**
11	5.0[d]	100	CH_3CN	25	62
12	5.0[d]	105	CH_3CN	30	68
13	5.0[d]	110	CH_3CN	30	65

[a] Conditions: cartridge-purified **^{18}F-2**, solvent (0.8–1.2 mL), manual addition of **3a** to the reaction vial of the synthesis module, **3a** was split into two equal batches and added portion-wise. [b] RCY was determined by radio-HPLC analysis of the crude product **^{18}F-JCN037**. [c] Crude **^{18}F-2**. [d] Automated addition of **3a** *via* the synthesis module.

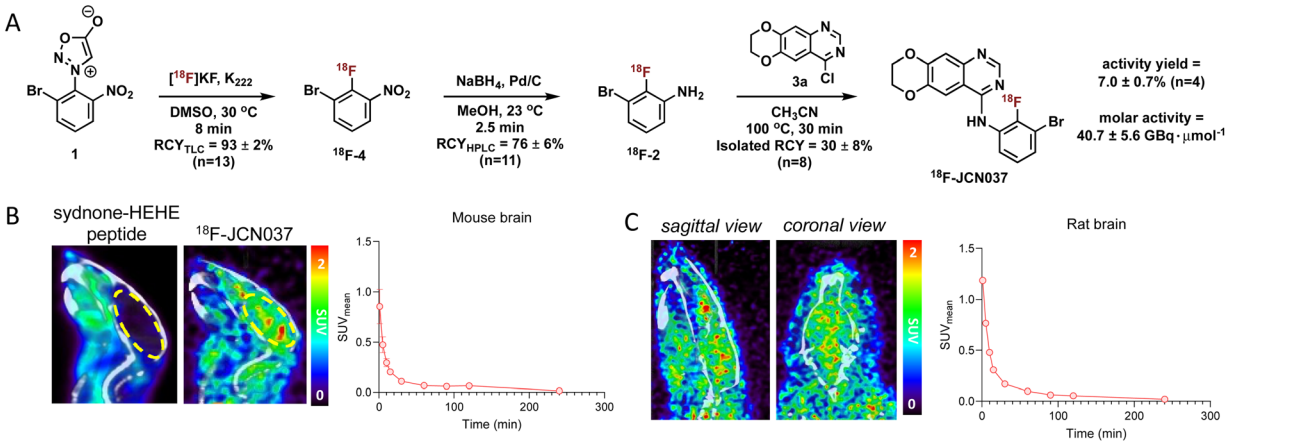

Fig. 2 (A) Radiosynthesis of **^{18}F-JCN037**. (B) Representative co-registered PET/CT images of sydnone-HEHE-peptide and brain-penetrant **^{18}F-JCN037** biodistribution in a mouse at 1 min post-injection of the tracer and the time–activity curve of **^{18}F-JCN037** in the mouse brain. (C) Representative co-registered PET/CT images of **^{18}F-JCN037** biodistribution in a rat brain at 5 min post-injection of the tracer and the associated time–activity curve.

the 4-chloroquinazoline to the reaction vial in an automated process. With acetonitrile as the solvent, treatment of **^{18}F-2** with 5.0 mg of **3a** at 100 °C for 30 min generated **^{18}F-JCN037** in 78% RCY (Table 3, entry 10).

Having optimized the synthetic protocol, we streamlined the process to ensure the production of **^{18}F-JCN037** on the ELIXYS radiosynthesis module, with minimal manual manipulation. The radiofluorination and substitution steps as well as the intermediate cartridge purifications were fully automated. The reduction step was conducted under inert atmosphere; as such, intermediate **^{18}F-4** was pushed into a sealed vial equipped with an argon balloon, situated on a stir plate next to the radiochemical synthesis module (Fig. S8†). Following the reduction, the vial was manually unscrewed and placed back into the ELIXYS for the completion of the automated synthesis. HPLC purification of **^{18}F-JCN037** was fully automated and the tracer was obtained in >99% radiochemical purity and 24 ± 5% isolated RCY, based on starting [^{18}F]fluoride activity (decay corrected, $n = 4$). The activity yield was 7.0 ± 0.7% (non-decay corrected, $n = 4$) and the molar activity was 40.7 ± 5.6 GBq μmol^{-1} (1.1 ± 0.1 Ci μmol^{-1}), ($n = 3$) (Fig. 2A).

Molecular imaging of ^{18}F-JCN037

To evaluate the biodistribution of JCN037 *in vivo*, preclinical imaging studies with **^{18}F-JCN037** were conducted. Micro-positron emission tomography-computed tomography (microPET/CT) imaging studies were performed in naïve C57BL6 mice and in a Sprague Dawley (SD) rat at 0–2 h (dynamic scan) and 4 h (static scan) post-injection (p.i.) of the tracer (Fig. 2). Rapid accumulation of **^{18}F-JCN037** was observed in the mouse brain, with a SUV_{mean} value of 0.85 at 1 min p.i., followed by a rapid decrease in the probe concentration in the brain (Fig. S12†). This data is consistent with the previously reported short half-life of JCN037 due to rapid clearance.[14a] Our laboratory recently reported work involving a cyclic peptide-based radiotracer, sydnone-HEHE-peptide, which fails to cross the BBB.[17] Focusing on brain distribution, we compared the PET/CT images between mice that were administered either sydnone-HEHE-peptide or **^{18}F-JCN037** (Fig. 2B). The stark contrast between the *in vivo* images further highlights the rapid brain uptake of **^{18}F-JCN037**. Finally, rapid accumulation of **^{18}F-JCN037** occurred in the rat brain, with a SUV_{mean} value of 1.19 at 1 min p.i., followed by rapid decrease in the brain (Fig. 2C).

Preparation of ^{18}F-ERAS-801

Encouraged by the imaging results of **^{18}F-JCN037** we next pursued the synthesis of **^{18}F-ERAS-801**. In an effort to secure a fully automated radiosynthesis of **^{18}F-ERAS-801**, the sodium borohydride reduction step to afford aniline **^{18}F-2** was revised and reoptimized. Nitroarene **^{18}F-4** was converted to the corresponding aniline *via* iron reduction in the presence of acetic acid.[18] Optimization of the iron reduction was completed and the process was fully automated on the ELIXYS radiosynthesis module to afford **^{18}F-2** in 83 ± 3 RCY (Tables S13 and S14†).

Synthesis of 4-chloroquinazoline core **3b** was achieved following published protocols[14b] and the previously optimized conditions for the S_NAr between aniline **^{18}F-2** and **3a** were applied to the system using **3b** as the appropriate 4-chloroquinazoline (Fig. 3A). Fine tuning of the reaction conditions revealed that **^{18}F-ERAS-801** was generated in acetonitrile at 105 °C in 4 min in 86% RCY, based on radio-HPLC analysis of the crude product (Table S16†). Unlike **3a**, the addition of **3b** was performed in one-pot and, after HPLC-purification, afforded **^{18}F-ERAS-801** in 31 ± 6 isolated RCY ($n = 9$) (Table S17†).

Production of **^{18}F-ERAS-801** *via* the three-step process was fully automated on the ELIXYS radiosynthesis module (Fig. S13†) and was achieved in >99% radiochemical purity and 22 ± 4% isolated RCY, based on starting [^{18}F]fluoride activity (decay corrected, $n = 9$). The activity yield of **^{18}F-ERAS-801** was 8 ± 2% (non-decay corrected, $n = 9$) and the molar activity was 41.8 ± 14.1 GBq μmol^{-1} (1.1 ± 0.4 Ci μmol^{-1}), ($n = 4$) (Fig. 3A). Inductively coupled plasma mass spectrometry (ICP-MS)

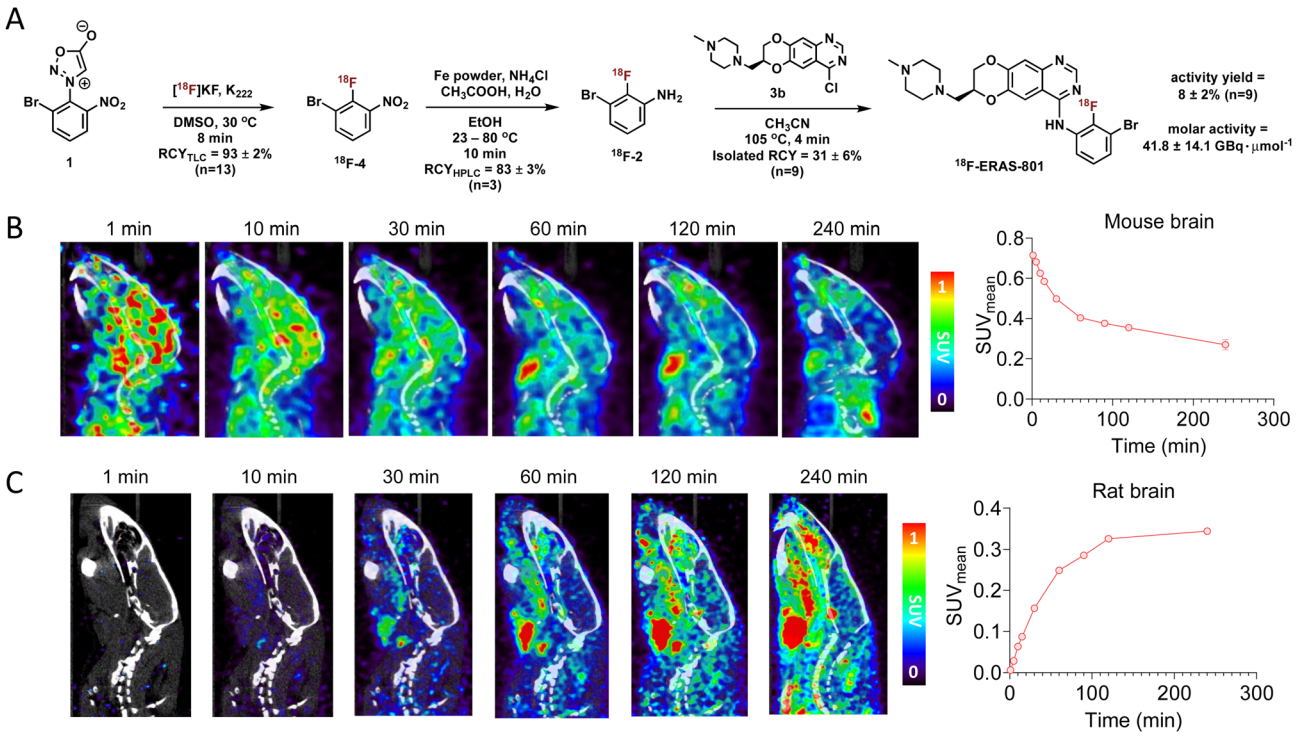

Fig. 3 (A) Radiosynthesis of ^{18}F-ERAS-801. (B) and (C) Representative co-registered PET/CT images of brain-penetrant ^{18}F-ERAS-801 biodistribution in (B) a mouse and (C) a rat at indicated timepoints post-injection of the tracer, with corresponding time–activity curves of ^{18}F-ERAS-801 uptake in the brains of each animal.

analysis was performed to detect iron in the formulated ^{18}F-ERAS-801 samples and the residual iron content was determined to be <10 ppb ($n = 2$ samples), which is well below the acceptable limit for in-human injection.[19] Additional quality control (QC) testing was performed on the formulated dose which met or exceeded the specified criteria for clinical applications (Table S21†).

Molecular imaging of ^{18}F-ERAS-801

With an automated synthesis of ^{18}F-ERAS-801 in hand, microPET/CT imaging studies were conducted in rodents to evaluate overall brain penetration and tissue accumulation of the radiotracer (Fig. 3). Rapid uptake of ^{18}F-ERAS-801 was observed in the mouse brain, with a SUV_{mean} value of 0.71 at 1 min p.i. followed by significantly improved retention and

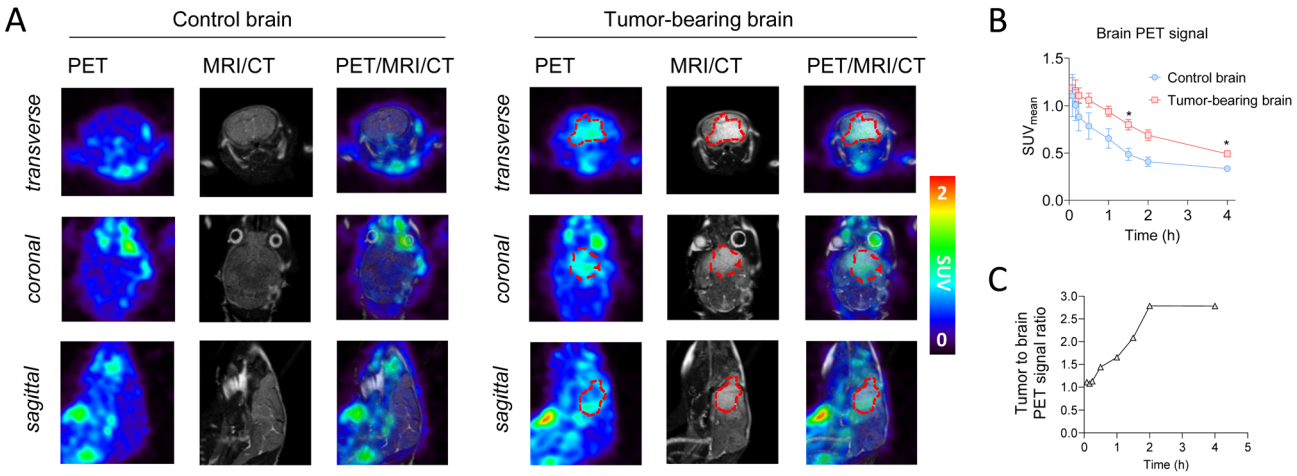

Fig. 4 (A) Representative co-registered PET/MRI/CT images of the control brain and the glioblastoma-bearing brain in mice, 4 hours post-injection of ^{18}F-ERAS-801. Dashed areas, glioblastoma. (B) Time-activity curves of ^{18}F-ERAS-801 in the healthy control mouse brain and in the glioblastoma-bearing mouse brain. (C) Tumor-to-brain ratio of ^{18}F-ERAS-801 uptake over 4 hours post-injection of the tracer. *$p < 0.05$.

a slower clearance than what was observed for **^{18}F-JCN037** (Fig. 3B). Remarkably, the *in vivo* biodistribution of **^{18}F-ERAS-801** in a SD rat revealed a slow initial uptake of the radiotracer in the rat brain, with a SUV_{mean} value of 0.33 at 2 h p.i., followed by a long retention time of activity in the brain at 4 h p.i. (Fig. 3C).

Encouraged by the significantly improved pharmacokinetic properties and brain retention of **^{18}F-ERAS-801**, microPET/CT imaging and biodistribution studies were conducted in mice with GliomaPDOX tumors implanted in the brain to assess targeting and sensitivity (Fig. 4). In parallel, non-tumor bearing NSG mice were evaluated as a control group. To better visualize the brain anatomy and the implanted glioblastoma, MRI was performed in addition to PET and CT due to its superior soft tissue contrast (Fig. 4A). The PET signal is significantly higher in the whole-brain of the tumor-bearing mice compared to the whole-brain of the healthy control mice (Fig. 4B). After 1 hour tracer uptake, **^{18}F-ERAS-801** displayed 1.7-fold higher PET signal in tumor tissue than healthy brain tissue, with relatively high retention in the tumor over the next three hours (Fig. 4C). Notably, at the 4-hour time point, **^{18}F-ERAS-801** accumulation was nearly 3-fold higher than tracer signal in the healthy tissue of the corresponding brain, confirming target specificity (Fig. 4C).

The greater uptake of **^{18}F-ERAS-801** in the brain suggests that ERAS-801 may overcome the poor BBB penetrating properties of other EGFR TKIs that have been tested and failed in GBM. It remains to be determined if these improved properties of ERAS-801 will translate into a clinical benefit for GBM patients. However, the improved outcomes for EGFR-mutant NSCLC patients with brain metastasis treated with the CNS penetrant EGFR TKI Tagrisso[20] suggests that higher brain exposures of an EGFR TKI can be effective and non-toxic in the brain.

Conclusions

In summary, we have developed two PET tracers, **^{18}F-JCN037** and **^{18}F-ERAS-801**, that are fluorine-18 isotopologues of JCN037 and its clinical derivative ERAS-801, recently developed TKIs against EGFR-driven GBM. PET imaging studies of these tracers enabled noninvasive, whole-body pharmacological measurements including brain accumulation and retention, valuable data for CNS drug development. The synthesis of **^{18}F-ERAS-801** was fully automated on a commercial radiosynthesis module in 8 ± 2% activity yield. PET imaging studies of **^{18}F-ERAS-801** confirmed BBB penetration and, importantly, provided insights into the intratumoral drug distribution in the brain for EGFR-driven GBM tumors.

PET tracers that can validate tumor engagement during preclinical drug development, visualize and quantify EGFR expression *in vivo*, differentiate between EGFR mutational statuses, and potentially predict patients' response to TKI treatment are of great interest. PET imaging was recently reported to enable precise quantification of EGFR mutation status in NSCLC patients and improve overall patient management and care.[8c] The beneficial role of **^{18}F-ERAS-801** to provide this type of predictive information for the clinical assessment of ERAS-801 treatment remains to be seen and additional studies are ongoing to validate this potential value.

Ethical statement

All mice were kept under defined pathogen-free conditions at the AAALAC-approved animal facility of the Division of Laboratory Animals at UCLA. All studies were in accordance with UCLA Office of Animal Resource Oversight (OARO) protocol guidelines and with UCLA Animal Research Committee protocol guidelines.

Data availability

Experimental procedures, optimization, characterization data, NMR spectra, *in vivo* imaging methods and analyses are available in the ESI.†

Author contributions

M. K. N. carried out the radiochemistry experiments and optimization with guidance from J. M. M. Imaging experiments were designed by S. X. and conducted by J. E. T. and S. X. with input from D. A. N. The manuscript was written by M. K. N. and J. M. M. and edited by all authors.

Conflicts of interest

M. K. N., J. E. T., D. A. N., and J. M. M. are inventors on a patent application covering chemical matter in this publication that is assigned to The Regents of the University of California. D. A. N. is a co-founder, shareholder and consultant for Katmai Pharmaceuticals, which has licensed IP related to this work.

Acknowledgements

Financial support was provided in part by the Crump Institute for Molecular Imaging and the Jonsson Comprehensive Cancer Center (JCCC) Career Development Seed Grant. The GNEXT microPET/CTscanner (Sofie Biosciences) was funded by an NIH Shared Instrumentation for Animal Research (SIFAR) Grant (1S10OD026917-01A1). The microPET/CT studies were supported in part by the JCCC Support Grant (2P30CA016042-44). We thank Jeffrey Collins for providing [^{18}F]fluoride for these studies and Mikayla Tamboline for performing the microPET/CT imaging studies.

Notes and references

1 R. Stupp, W. P. Mason, M. J. van den Bent, M. Weller, B. Fisher, M. J. B. Taphoorn, K. Belanger, A. A. Brandes, C. Marosi, U. Bogdahn, J. Curschmann, R. C. Janzer, S. K. Ludwin, T. Gorlia, A. Allgeier, D. Lacombe, J. G. Cairncross, E. Eisenhauer and R. O. Mirimanoff, *N. Engl. J. Med.*, 2005, **352**, 987–996.

2 (*a*) K. Kobayashi and K. Hagiwara, *Targeted Oncology*, 2013, **8**, 27–33; (*b*) P. Ballard, J. W. T. Yates, Z. Yang, D.-W. Kim,

J. C.-H. Yang, M. Cantarini, K. Pickup, A. Jordan, M. Hickey, M. Grist, M. Box, P. Johnström, K. Varnäs, J. Malmquist, K. S. Thress, P. A. Jänne and D. Cross, *Clin. Cancer Res.*, 2016, **22**, 5130–5140.

3 (*a*) A. B. Lassman, M. R. Rossi, J. R. Razier, L. E. Abrey, F. S. Lieberman, C. N. Grefe, K. Lamborn, W. Pao, A. H. Shih, J. G. Kuhn, R. Wilson, N. J. Nowak, J. K. Cowell, L. M. DeAngelis, P. Wen, M. R. Gilbert, S. Chang, W. A. Yung, M. Prados and E. C. Holland, *Clin. Cancer Res.*, 2005, **11**, 7841–7850; (*b*) I. Vivanco, H. I. Robins, D. Rohle, C. Campos, C. Grommes, P. L. Nghiemphu, S. Kubek, B. Oldrini, M. G. Chheda, N. Yannuzzi, H. Tao, S. Zhu, A. Iwanami, D. Kuga, J. Dang, A. Pedraza, C. W. Brennan, A. Heguy, L. M. Liau, F. Lieberman, W. K. A. Yung, M. R. Gilbert, D. A. Reardon, J. Drappatz, P. Y. Wen, K. R. Lamborn, S. M. Chang, M. D. Prados, H. A. Fine, S. Horvath, N. Wu, A. B. Lassman, L. M. DeAngelis, W. H. Yong, J. G. Kuhn, P. S. Mischel, M. P. Mehta, T. F. Cloughesy and I. K. Mellinghoff, *Cancer Discovery*, 2012, **2**, 458–471.

4 W. M. Pardridge and J. Cereb, *Blood Flow Metab.*, 2012, **32**, 1959–1972.

5 (*a*) R. Uppoor, P. Mummaneni, E. Cooper, H. Pien, A. Sorensen, J. Collins, M. Mehta and S. Yasuda, *Clin. Pharmacol. Ther.*, 2008, **84**, 69–74; (*b*) P. M. Matthews, E. A. Rabiner, J. Passchier and R. N. Gunn, *Br. J. Clin. Pharmacol.*, 2012, **73**, 175–186.

6 L. Cunha, K. Szigeti, D. Mathé and L. F. Metello, *Drug Discovery Today*, 2014, **19**, 936–948.

7 O. Gefvert, M. Bergström, B. Långström, T. Lundberg, L. Lindström and R. Yates, *Psychopharmacology*, 1998, **135**, 119–126.

8 (*a*) P. Slobbe, A. J. Poot, A. D. Windhorst and G. A. M. S. van Dongen, *Drug Discovery Today*, 2012, **17**, 1175–1187; (*b*) V. Bernard-Gauthier, J. J. Bailey, S. Berke and R. Schirrmacher, *Molecules*, 2015, **20**, 22000–22027; (*c*) X. Sun, Z. Xiao, G. Chen, Z. Han, Y. Liu, C. Zhang, Y. Sun, Y. Song, K. Wang, F. Fang, X. Wang, Y. Lin, L. Xu, L. Shao, J. Li, Z. Cheng, S. S. Gambhir and B. Shen, *Sci. Transl. Med.*, 2018, **10**, eaan8840; (*d*) E. A. van de Stadt, M. Yaqub, A. A. Lammertsma, A. J. Poot, P. R. Schober, R. C. Schuit, E. F. Smit, I. Bahce and N. H. Hendrikse, *EJNMMI Res.*, 2020, **10**, 97; (*e*) A. Högnäsbacka, A. J. Poot, D. J. Vugts, G. A. M. S. van Dongen and A. D. Windhorst, *Pharmaceuticals*, 2022, **15**, 450; (*f*) E. Van De Stadt, M. Yaqub, A. A. Jahangir, H. Hendrikse and I. Bahce, *Front. Oncol.*, 2022, **12**, 900450.

9 (*a*) T. Läppchen, M. L. H. Vlaming, E. Custers, J. Lub, C. F. Sio, J. DeGroot and O. C. Steinbach, *Appl. Radiat. Isot.*, 2012, **70**, 205–209; (*b*) Y. Seimbille, M. E. Phelps, J. Czernin and D. H. S. Silverman, *J. Labelled Compd. Radiopharm.*, 2005, **48**, 829–843.

10 H. Su, Y. Seimbille, G. Z. Ferl, C. Bodenstein, B. Fueger, K. J. Kim, Y.-T. Hsu, S. M. Dubinett, M. E. Phelps, J. Czernin and W. A. Weber, *Eur. J. Nucl. Med. Mol. Imaging*, 2008, **35**, 1089–1099.

11 N. J. Taylor, E. Emer, S. Preshlock, M. Schedler, M. Tredwell, S. Verhoog, J. Mercier, C. Genicot and V. Gouverneur, *J. Am. Chem. Soc.*, 2017, **139**, 8267–8276.

12 P. Slobbe, A. D. Windhorst, M. S.-v. Walsum, R. C. Schuit, E. F. Smit, H. G. Niessen, F. Solca, G. Stehle, G. A. M. S. van Dongen and A. J. Poot, *Nucl. Med. Biol.*, 2014, **41**, 749–757.

13 (*a*) P. Slobbe, A. D. Windhorst, M. Stigter-van Walsum, E. F. Smit, H. G. Niessen, F. Solca, G. Stehle, G. A. M. S. van Dongen and A. J. Poot, *EJNMMI Res.*, 2015, **5**, 14; (*b*) N. Colclough, K. Chen, P. Johnström, N. Strittmatter, Y. Yan, G. L. Wrigley, M. Schou, R. Goodwin, K. Varnäs, S. J. Adua, M. Zhao, D. X. Nguyen, G. Maglennon, P. Barton, J. Atkinson, L. Zhang, A. Janefeldt, J. Wilson, A. Smith, A. Takano, R. Arakawa, M. Kondrashov, J. Malmquist, E. Revunov, A. Vazquez-Romero, M. M. Moein, A. D. Windhorst, N. A. Karp, M. R. V. Finlay, R. A. Ward, J. W. T. Yates, P. D. Smith, L. Farde, Z. Cheng and D. A. E. Cross, *Clin. Cancer Res.*, 2021, **27**, 189–201.

14 (*a*) J. E. Tsang, L. M. Urner, G. Kim, K. Chow, L. Baufeld, K. Faull, T. F. Cloughesy, P. M. Clark, M. E. Jung and D. A. Nathanson, *ACS Med. Chem. Lett.*, 2020, **11**, 1799–1809; (*b*) D. A. Nathanson, M. E. Jung, J. E. Tsang, L. M. Urner, P. M. Clark, T. F. Cloughesy and G. Kim, *US Pat.*, US011377451B011377452, 2022.

15 (*a*) B. H. Rotstein, N. A. Stephenson, N. Vasdev and S. H. Liang, *Nat. Commun.*, 2014, **5**, 4365; (*b*) A. V. Mossine, A. F. Brooks, K. J. Makaravage, J. M. Miller, N. Ichiishi, M. S. Sanford and P. J. H. Scott, *Org. Lett.*, 2015, **17**, 5780–5783; (*c*) L. S. Sharninghausen, A. F. Brooks, W. P. Winton, K. J. Makaravage, P. J. H. Scott and M. S. Sanford, *J. Am. Chem. Soc.*, 2020, **142**, 7362–7367.

16 M. K. Narayanam, G. Ma, P. A. Champagne, K. N. Houk and J. M. Murphy, *Angew. Chem., Int. Ed.*, 2017, **56**, 13006–13010.

17 M. K. Narayanam, B. T. Lai, J. M. Loredo, J. A. Wilson, A. M. Eliasen, N. A. LaBerge, M. Nason, A. L. Cantu, B. K. Luton, S. Xu, H. D. Agnew and J. M. Murphy, *Bioconjugate Chem.*, 2021, **32**, 2073–2082.

18 D. C. Whritenour, S. J. Brenek and N. J. Tom, *Org. Process Res. Dev.*, 2001, **5**, 539–541.

19 Guidelines for Elemental Impurities, **https://www.ema.europa.eu/en/ich-q3d-elemental-impurities-scientific-guideline**, accessed 12-April-2023.

20 T. S. Mok, Y.-L. Wu, M.-J. Ahn, M. C. Garassino, H. R. Kim, S. S. Ramalingam, F. A. Shepherd, Y. He, H. Akamatsu, W. S. M. E. Theelen, C. K. Lee, M. Sebastian, A. Templeton, H. Mann, M. Marotti, S. Ghiorghiu and V. A. Papadimitrakopoulou, *N. Engl. J. Med.*, 2017, **376**, 629–640.